



Multifunctional nanoprobes based on upconverting lanthanide doped CaF₂: towards biocompatible materials for biomedical imaging

Journal:	<i>Biomaterials Science</i>
Manuscript ID:	BM-ART-04-2014-000119.R1
Article Type:	Paper
Date Submitted by the Author:	19-May-2014
Complete List of Authors:	<p>Cantarelli, Irene; Università di Verona, Dipartimento di Biotecnologie Pedroni, Marco; Università di Verona, Dipartimento di Biotecnologie Piccinelli, Fabio; University of Verona, Dipartimento di Biotecnologie Marzola, Pasquina; Università di Verona, Dipartimento di Informatica Boschi, Federico; Univerity of verona, Dipartimento di Informatica Conti, Giamaica; Università di Verona, Dipartimento di Scienze Neurologiche e del Movimento Sbarbati, Andrea; Università di Verona, Dipartimento di Scienze Neurologiche e del Movimento Bernardi, Paolo; Università di Verona, Dipartimento di Scienze Neurologiche e del Movimento Mosconi, Elisa; Università di Verona, Dipartimento di Scienze Neurologiche e del Movimento Perbellini, Luigi; Università di Verona, Dipartimento di Sanità Pubblica e Medicina di Comunità Marongiu, Laura; Università di Verona, Dipartimento di Patologia e Diagnostica, Sezione di Patologia Generale Donini, Marta; Università di Verona, Dipartimento di Patologia e Diagnostica, Sezione di Patologia Generale Dusi, Stefano; Università di Verona, Dipartimento di Patologia e Diagnostica, Sezione di Patologia Generale Sorace, Lorenzo; Università di Firenze, INSTM and Dipartimento di Chimica "U. Schiff" Innocenti, Claudia; Università di Firenze, INSTM and Dipartimento di Chimica "U. Schiff" Fantechi, Elvira; Università di Firenze, INSTM and Dipartimento di Chimica "U. Schiff" Sangregorio, Claudio; Università di Firenze, Dipartimento di Chimica Speghini, Adolfo; University of Verona, Department of Biotechnology</p>

ARTICLE

Multifunctional nanoprobes based on upconverting lanthanide doped CaF₂: towards biocompatible materials for biomedical imaging

Cite this: DOI: 10.1039/x0xx00000x

Received 00th January 2012,
Accepted 00th January 2012

DOI: 10.1039/x0xx00000x

www.rsc.org/

Irene Xochilt Cantarelli^a, Marco Pedroni^a, Fabio Piccinelli^a, Pasquina Marzola^b, Federico Boschi^b, Giamaica Conti^c, Andrea Sbarbati^c, Paolo Bernardi^c, Elisa Mosconi^c, Luigi Perbellini^d, Laura Marongiu^e, Marta Donini^e, Stefano Dusi^e, Lorenzo Sorace^f, Claudia Innocenti^f, Elvira Fantechi^f, Claudio Sangregorio^g, Adolfo Spgehini^{a*}

Water dispersible Gd³⁺, Yb³⁺, Er³⁺ and Gd³⁺, Yb³⁺, Tm³⁺ doped CaF₂ nanoparticles (NPs) were prepared by a one-pot hydrothermal synthesis using citrate ions as capping agents without the need of any post-synthesis reaction. UC emissions are easily observed in the visible and infrared regions upon NIR diode laser excitation at 980 nm. EPR spectroscopy confirms the substitutional nature of the rare-earth doping, while magnetometric studies reveal that the NPs have a useful magnetization. MRI experiments conducted *in vivo*, show that after 40 min from the injection the NPs localize in the liver and spleen. Electron microscopy images of liver tissue reveals that the NPs are located in the Kupffer cells, although a small amount are also found in the hepatocytes. An excitation with a 980 emission on the excises liver and epithelial tissue induce clearly visible UC emission. The local temperature upon 980 nm irradiation was monitored in-situ and it was found to increase slowly with the exposure time, maintaining under 1-2 °C for less than 60 seconds exposures. The NPs have a low toxicity on cultured He-La cells and human primary dendritic cells (DCs), and did not induce pro-inflammatory cytokine secretion by cultured human DCs, indicating that the NPs do not cause relevant adverse reactions in immune cells. Therefore, the present NPs are suitable candidates to be efficiently used in surgery applications, where spatial resolution and lack of harmful effects on human health are important issues.

1. Introduction

Multimodal bioimaging is a challenging research frontier in biology and medicine, and is becoming a technique of paramount importance in medical diagnostics¹, with particular relevance in the early diagnosis of tumors²⁻⁵. In this respect, nanostructured materials have a very important role thanks to their intrinsic small size that permits their easy incorporation as probes in living cells or organisms^{1,6,7}. The possible functionalization of the nanostructured materials further opens the possibility to guide them towards well-defined targets in the living body, such as tumors or other localized lesions^{2-5,8,9}. In the recent years, important efforts have been made to develop new nanostructured materials able to combine more than one

imaging modalities, such as optical and Magnetic Resonance Imaging (MRI), X-ray computed tomography (CT) and positron emission tomography (PET)¹⁰⁻¹³. In this contest, multimodal probes combining magnetic and optical properties are particularly appealing. The MRI technique presents not only superb soft tissue contrast and good spatial resolution but also high penetration depth since biological tissues are essentially transparent to magnetic fields¹⁴. Moreover, the MRI tool can provide important information to clinical surgery in term of images with excellent anatomical details that can be acquired in short time intervals, such as minutes or below. Nevertheless, drawbacks of MRI are related to limited sensitivity and poor resolutions for imaging at cellular level. On the contrary, optical imaging is characterized by high sensitivity and sub-

micrometer resolution. Hence, nanostructured materials with both optical and MRI abilities can combine the advantages of each technique, in terms of imaging resolution and penetration depth.

In this scenario, lanthanide based or doped nanostructured inorganic materials represent very interesting probes in medical diagnostics for their well-known luminescent and magnetic properties^{9,15-21}, deriving from their peculiar electronic structure. In the last years, lanthanide doped oxide and fluoride nanoparticles (NPs) have been the subject of many investigations^{9,19-25}. Among these materials, lanthanide doped upconverting (UC) NPs (UCNPs) gained attention in biomedical imaging due to their peculiar properties²⁶. The UC process, relevant to the Ln^{3+} ions, involves the conversion of low energy excitation radiation (typically near-infrared, NIR) to higher energies and can be obtained using inexpensive continuous wave diode NIR lasers (e.g. at 980 nm) as the excitation source. NIR-to-NIR or NIR-to-red UC is particularly suitable for biomedical imaging as both the exciting and emitted radiations lie on the so-called first biological window of tissue transparency (650-1000 nm), in which the absorption of the biological tissues is very low, therefore ensuring a high degree of optical penetration^{27,28}.

Lanthanide ions are also useful as paramagnetic contrast agents, due to unpaired electrons in their 4f orbitals. Gd-based molecular complexes, such as Gd-DOTA or Gd-DTPA are among the most diffuse MRI contrast agents^{29,30}. On the other hand, fluoride and oxide nanostructures containing Gd^{3+} ions, such as Gd_2O_3 ³¹⁻³³, GdPO_4 ^{34,35}, GdVO_4 ³⁶, GdF_3 ^{11,12,37-39}, NaGdF_4 ^{20,40}, KGdF_4 ^{41,42}, and also Gd^{3+} doped NaYF_4 ^{19,21,25,43} or NaLuF_4 ⁴⁴⁻⁴⁶ are reported to have significant positive or negative MRI capabilities. UC properties can be added to such MRI active nanostructures using suitable combinations and concentrations of luminescent lanthanide ions (e.g. Er/Yb or Tm/Yb)^{26,44,47-55}. We indicate hereafter these nanostructured materials as MRI/UCNPs.

Taking advantage of these optical/magnetic multimodal bioprobes, the “real time evolution therapy” could be in principle possible. In the case of cancer surgery, the MRI/UCNPs, possibly conjugated with tumor-specific antibodies, could be injected intravenous or locally in order to target the tumor. At first stage, the bimodal NPs can localize the tumor, within a few millimeters, through an *in-vivo* fast and non-invasive MRI scan. Then, the MRI/UCNPs could be supervised during the surgery, in the cancerous region, using a common NIR diode laser with sub-millimeter spatial resolution, guiding exactly the surgeon to excise the mass. This technique based on “see-treat-see” the injury opens the way to a fast surgical treatment of the tumor and to its precise and complete physical elimination, a result obtained combining the two imaging modalities and thus overcoming the limitations of single modal optical and MRI techniques.

From the design strategy point of view, multimodal NPs can be generally classified in two categories based on their structures: core/shell and single phase NPs. Important efforts have been recently dedicated to the synthesis of core/shell nanomaterials,

such as $\text{NaYbF}_4\text{:Tm/NaGdF}_4$ ⁵⁶, $\text{NaGdF}_4\text{:Yb,Er/SiO}_2$ ^{57,58}, $\text{NaYF}_4\text{:Yb,Tm/NaGdF}_4$ ⁵⁹, $\text{NaYF}_4\text{:Er,Yb/NaGdF}_4$ ^{53,60} and $\text{GdVO}_4\text{:Yb,Er(Ho,Tm)/SiO}_2$ ³⁶ and $\text{NaLuF}_4\text{:Yb,Tm@NaGdF}_4$ ^(¹⁵³Sm)²⁰, $(\text{NaYF}_4\text{:20%Yb/2%Tm/15%Gd@NaGdF}_4)$ ²¹. The preparation of the core/shell structures typically occurs through a multi-step sequence, which could be complicated and time-consuming. By contrast, single-phase multimodal NPs can be prepared by facile one-step routes, by co-doping magnetic and luminescent lanthanide ions in single hosts by solvothermal or coprecipitation methods. Examples of incorporation of lanthanide ions in single phase MRI/UCNPs are $\text{SrF}_2\text{:Yb,Er,Gd}$ ⁶¹, $\text{GdF}_3\text{:Yb,Er,Gd}$ and $\text{GdF}_3\text{:Yb,Tm,Gd}$ ¹³, $\text{NaYF}_4\text{:Yb,Er,Gd}$ ^{19,25,60}, $\text{NaLuF}_4\text{:Yb,Tm,Gd}$ ⁴⁴, $\text{NaGdF}_4\text{:Yb,Tm}$ ^{9,62}, $\text{NaGdF}_4\text{:Yb,Tm,Er}$ ⁴⁸, $\text{KGdF}_4\text{:Yb,Tm}$ ^{51,63} and $\text{GdPO}_4\text{:Yb,Tb}$ ³⁵.

It is worth to remark that simple, low-cost, environmental friendly synthetic pathways for the synthesis of the nanostructured materials, while maintaining efficient imaging capabilities, is of paramount importance for environmental sustainability. Moreover, biocompatibility, toxicity and long-term stability are also very important features that need to be fulfilled for *in-vivo* biomedical imaging application of the NPs. In fact, a major problem hampering the use of NPs for medical applications is the ability of some nanostructures to stimulate immune cells, such as dendritic cells (DCs), to release proinflammatory cytokines that trigger hypersensitivity reactions and inflammation leading to harmful effects on human health⁶⁴⁻⁶⁷. DCs are a heterogeneous cell population that capture antigens in peripheral tissues and then migrate to lymph nodes to present antigens to lymphocytes and to activate the specific T cell immunity⁶⁸. DCs produce various cytokines that orchestrate the inflammatory and immune response, such as IL-12 that plays a key role in the activation of natural killer cells and T lymphocytes, which in turn release immune regulatory mediators⁶⁹ and IL 23 that induces T cells to produce pro-inflammatory chemical mediators⁷⁰. Moreover DCs release IL-6, IL-1 β , and TNF- α that show pro-inflammatory and immune stimulatory effects and play a prominent role in the induction of systemic acute phase reaction, characterized by fever, headache, changes in sleep-wake cycle, anorexia, inactivity, nausea and emesis⁷¹⁻⁷³. Therefore to be suitable candidates for biomedical purposes NPs should not induce DCs to produce cytokines leading to inflammation and/or to immune system derangement promoting an increased incidence of autoimmune and allergic diseases^{74,75}.

The present investigation involves saline dispersible $\text{CaF}_2\text{:Gd,Yb,Er}$ and $\text{CaF}_2\text{:Gd,Yb,Tm}$ UCNPs, with the aim to achieve efficient, biologically compatible nanostructured platforms for fast multimodal imaging in medical diagnostics.

2. Experimental section

2.1 Synthesis details

Lanthanide tri-doped CaF₂ NPs were synthesized by a hydrothermal method developed by our group²⁷. Briefly, stoichiometric amounts of the metal chlorides GdCl₃·6H₂O (Aldrich 99.99 %), CaCl₂·2H₂O, ErCl₃·6H₂O, YbCl₃·6H₂O and TmCl₃·6H₂O (Aldrich 99.9 %) were dissolved in 7 ml of deionized water (total metal amount equal to 3.5 mmol) and Ca:Gd:Yb:Er = 70:15:12:3 or Ca:Gd:Yb:Tm = 70:15:14:1 molar ratios. To this solution, 20.0 ml of potassium citrate (1 M) and 3.0 ml of NH₄F (3.5 M, Aldrich, 99.9 %) solutions were added. The resultant clear solution was heated in a 50 ml stainless steel Teflon lined digestion Pressure Vessel (DAB-2, Berghof) at 190 °C for 6 h. After washing with acetone and drying at room temperature, the obtained NPs were directly dispersed in water. The dispersions remained stable for several weeks. Samples with lower concentration of Gd³⁺ ions (Ca:Gd:Yb:Er = 70:8:20:2) have been prepared for further EPR measurements.

2.2 X-Ray powder diffraction setup

X-Ray powder diffraction (XRPD) patterns were measured with a powder diffractometer (Thermo, ARL XTRA), operating in Bragg-Brentano geometry, equipped with a Cu-anode X-ray source (K_{α} =1.5418 Å) and using a Peltier Si(Li) cooled solid state detector. The patterns were collected at a scan rate of 0.04 °/sin the 15°-90° 2θ range. The powdered samples were finely ground in a mortar and then deposited in a low-background sample stage for the measurements.

2.3 TEM images

The size and morphology of the NPs were analyzed by transmission electron microscopy (TEM) technique, using a CM12 Philips microscope operating at 100 kV. Samples were prepared by drop drying a dilute suspension of the NPs onto 200 mesh carbon-coated copper grids. The recorded micrographs were further analyzed with the Image Pro-Plus© software. The mean diameter and size distribution of each sample were obtained from a statistical analysis over ca. 800 NPs.

A portion of liver, excised after MRI experiments, was fixed with glutaraldehyde 2.5% in 0.1M phosphate buffer, pH 7.4 at 4°C for 3 h. Hence, they were postfixed in osmium tetroxide 1% for 1 hour in the same buffer, dehydrated in graded acetones (60–100%), embedded in Epon-Araldite and cut with an Ultracut ultramicrotome (Reichert, Wien, Austria). Ultrathin sections unstained were observed with a Philips Morgagni transmission electron microscope (FEI Company Italia Srl, Milano, Italy) operating at 80 kV and equipped with a Megaview II camera for digital image acquisition.

2.4 ICP-MS analysis

Mineralization was carried out with a microwave digestion system MARS XPRESS (CEM Corporation, North Carolina, USA) equipped with 10 ml Teflon PFA by adding 0.8 ml of nitric acid (Optima grade for ultra-low trace metal analysis from Fisher Scientific) and 1.1 ml high-purity water (Milli-Q apparatus, Millipore, Milan) to 0.1 ml of NPs solution. The

samples were heated for 10 min at 80 °C, for 10 min at 120 °C and then for 20 min at 180°C. After cooling at room temperature the obtained samples were transferred in polypropylene tubes and stored at -20°C until analysis. For ICP-MS analysis 0.1 mL of the digested sample was diluted by adding 4.90 mL Milli-Q water. External calibration solutions (10 to 400 µg/L) were prepared by diluting 10 mg/L multi-elemental standard solution. 2 µg/L rhodium was used as internal standard. ICP-MS measurements were performed using a Thermo Fisher Scientific model X Series II equipped with a technology collision/reaction cell (CCT) and an ASX 520 autosampler (Cetac Technologies, Omaha, NB).

2.5 Dynamic Light Scattering measurements

Dynamic Light Scattering (DLS) measurements were carried out using a Malvern Zetasizer Nano ZS90 operating with a He-Ne laser at 633 nm. Measurements were carried out in water colloidal dispersions of the CaF₂ NPs with a 0.5 g/L concentration.

2.6 Magnetic measurements

Magnetic measurements were performed using a Cryogenic S600 SQUID magnetometer operating in the 1.8-300 K temperature range and with an applied field up to 6.5 T. All data were corrected for the diamagnetic contribution of the sample holder. Powder X-band Electron paramagnetic resonance (EPR) spectra were recorded at variable temperature using a Bruker Elexsys E500 spectrometer with a 100 KHz frequency field modulation.

2.7 Upconversion spectra and temperature measurements

UC spectra were measured upon continuous wave laser excitation at 980 nm using a diode laser (1 W, MDL-III-980, CNI Optoelectronics Tech). The laser power was measured with a thermal power meter (S302C sensor, Thorlab). The emission signal was analyzed using a half-meter monochromator (HR460, Jobin Yvon) equipped with a 1200 lines/mm grating and detected with a CCD detector (Spectrum One, Jobin Yvon). The spectral resolution of the UC spectra is 0.1 nm. The UC luminescence pictures under ambient light illumination were acquired using a Canon CCD camera. A microscope objective (mod. 4608, Leika) was used to focus the 980 nm laser radiation. An optical chopper (SR540, Stanford Research Systems) with a 5/6 slot chopper blade was used for some UC measurements. The focused laser spot size was 0.5 mm. Temperature measurements were carried out using the UC emissions (see below) and an infrared camera (FLIR i7).

2.8 Cytotoxicity investigations

Cytotoxicity was studied by MTT test performed on HeLa cells cultured on 96 well plate. Cell were cultured with Dulbecco's Modified Eagle Medium (DMEM) added by 10% Fetal Bovine Serum (FBS) and 1% of antibiotic mix (penicillin/streptomycin 1:1 v/v). The plate was incubated for 24 hours at 37°C and 5% of CO₂. When at confluence, the growth medium was discarded and substituted with medium containing 1:20 and 1:50 diluted

NPs (stock colloidal dispersion were 1 % wt). The viability of cells was determined with the addition of 100 μ l of 3-(4,5-dimethyl-2-thiazolyl)-2,5-diphenyl-2H-tetrazolium bromide (MTT) in the growth medium, which was internalized by living cells and converted into insoluble Formazan resulting from the cellular ATP production. The concentration of living cells was determined by absorption measurements at 590 nm, after 6 hours of incubation of the HeLa cells with the NPs.

2.9 MRI setup and methods

MR imaging experiments were carried out using a Biospec Tomograph System (Bruker, Karlsruhe, Germany) equipped with a 4.7 Tesla, 33 cm bore horizontal magnet (Oxford Ltd, UK). A 72 mm internal diameter birdcage volume coil was used. Longitudinal (r_1) and transversal (r_2) relaxivities were measured in vitro using imaging sequences according to Passuello et al.¹³. For in vivo experiments, two Balb/c, male mice (6-8 weeks old) were intravenously injected with the CaF₂ NPs at the dosage of 6 mg of Gd per kg, corresponding to 38 μ mol/Kg, lower than the typical clinical dosage value for Gd-DTPA. For MRI acquisitions, animals were anesthetized with gas (a mixture of O₂ and air containing 1-1.5% of isoflurane), placed in a heated animal bed and inserted in a 3.5 cm internal diameter bird-cage coil. T₂-weighted images of the mouse body were acquired at 4.7 Tesla using a T₂-weighted sequence with the following parameters: FOV= 6x3 cm², MTX = 128x128 pixels, Slice thickness= 0.2 cm, TE= 5.9 ms TR= 2000 ms NEX=2, Echos=16. T₂* weighted images were also acquired using a Gradient-Echo sequence with the following parameters: TE= 4.4 ms, TR=1000 ms, FOV 6X3 cm², NEX= 2, MTX= 128X128, Slice Thickness=0.2 cm, angle=30°. The images were acquired before, 20 and 40 min after the NPs injection. Furthermore, a volume of 250 μ l of a colloidal dispersion of CaF₂ NPs was subcutaneously injected in a region of the mouse left posterior leg. After the MRI investigation, the mice were sacrificed by CO₂ and the liver and a section of the skin in the region of the subcutaneous injection of the NPs were excised. Both surgical samples were illuminated using the beam of a 980 nm diode laser, and images were obtained with a digital camera under natural light. A spectral filter (cut-off at 900 nm) was used to reject the diffused laser light. A further group of five mice were injected intravenously with the same dosage of the NPs under investigation and housed in temperature and humidity controlled environment for one month in order to monitor the health status for prolonged periods. This group of mice was not monitored by MRI technique. In vivo studies were conducted according to the guidelines of the Committee for Animal Research at the University of Verona.

2.10 Two-photon imaging

Two-photon UC images were acquired with a confocal Leica TCS SP5 System, using a Coherent Chameleon-Ultra Ti:sapphire pulsed laser. The NPs were excited at 975 nm and visualized with a 20x objective (water immersed, numerical aperture 1, Gain=59% e Filter wheel (FW)=40) in the range 500–600 nm (first channel) and 600-700 nm (second channel). The LAS AF (Leica Application Suite Advance Fluorescence) (Leica) software was used to process, archive and analyze the image data. For the two-photon measurements, excised liver samples were fixed in a 2% water solution of glutaraldehyde and paraffin embedded for histological sections preparation. Histological slices were dehydrated in xylene for 5 min and dry at 37°C overnight.

2.11 Preparation and culture of monocytes and DCs

After written informed consent and upon approval of the ethical committee, human blood was collected from healthy volunteers at the blood bank of the University of Verona. Monocytes were isolated from buffy coats by Ficoll-Hypaque and Percoll (GE Healthcare Life Science) density gradients and purified using the human monocyte isolation kit II (Miltenyi Biotec). The final monocyte population was 99% pure, as measured by FACS analysis. To generate DCs, monocytes were incubated at 37°C in 5% CO₂ for 5-6 days at 1 x 10⁶/ml in 6-well tissue culture plates (Greiner, Nürtingen, Germany) in RPMI 1640, supplemented with heat-inactivated 10% low endotoxin FBS, 2 mM L-glutamine, 50 ng/ml GM-CSF, and 20 ng/ml IL-4. The final DC population was 98% CD1a⁺, as measured by FACS analysis.

2.12 Evaluation of cell viability and analysis of cytokine production

The percentage of alive cells was determined using Annexin V staining kit (Miltenyi Biotec) in DCs and monocytes according to the manufacturer's instructions. Samples were acquired on a seven-color MACSQuant Analyzer (Miltenyi Biotec) and analysis performed by FlowJo software (TreeStar, Ashland, OR, USA).

Cytokine production in culture supernatants was determined by ELISA kits according to the manufacturer's instructions: IL-6 (range 8-800 pg/ml), IL-12 (range 4-500 pg/ml), IL-1 β (range 4-500 pg/ml), IL-23 (range 15-2000 pg/ml), TNF- α (range 4-500 pg/ml), purchased from eBioscience (San Diego, CA).

Ultrapure lipopolysaccharide (LPS, 0111: B4 strain) from *E. coli* was purchased from InvivoGen (San Diego, CA) and was used as positive control.

3. Results and discussion

Figure 1 shows the XRPD patterns for the tri-doped CaF_2 :Gd,Er,Yb and CaF_2 :Gd,Tm,Yb NPs, revealing that all the calcium fluoride NPs are single phase. The peak positions and intensities closely match those of the XRPD pattern for cubic CaF_2 powders (space group n. 225, $Fm-3m$), shown in Figure 1.

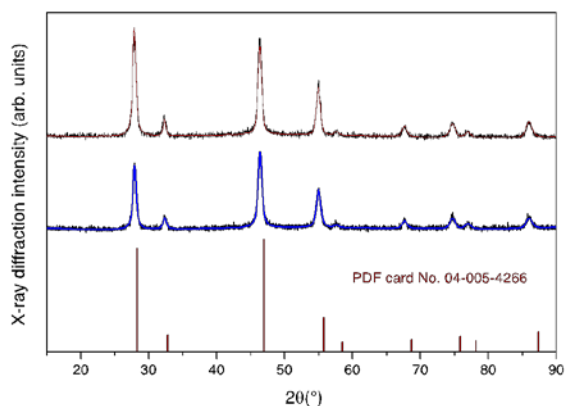


Figure 1. XRPD pattern for the CaF_2 :Gd,Yb,Tm (upper graph) and CaF_2 :Gd,Yb,Er (lower graph) NPs. Vertical lines: PDF card pattern n.04-005-4266 (cubic CaF_2 , space group n. 225, $Fm-3m$).

From a Rietveld refinement under the isotropic crystallite shape assumption for the two samples, crystal lattice parameters were obtained, reported in Table 1. As already observed for lanthanide doped CaF_2 NPs, the expansion of the unit cell volume for the present samples with respect to undoped CaF_2 hosts is due to the repulsion of the fluoride anions which play the role of charge compensators and which are also distributed in interstitial sites⁷⁶. Nonetheless, the dopant lanthanide ions substituting for Ca^{2+} ions in the fluorite structure can form clusters such as hexamers^{76, 77}.

Table 1. Unit cell parameters and isotropic particle size for single phase (cubic, space group n. 225) CaF_2 :Gd,Er,Yb NPs as obtained from a Rietveld refinement.

Sample	a (Å)	Unit cell volume (Å ³)	Particle size (nm)
CaF_2 ⁷⁸	5.463(1)	163.04(1)	---
CaF_2 :Gd,Er,Yb	5.539(1)	169.94(1)	18(1)
CaF_2 :Gd,Tm,Yb	5.537(1)	169.75(1)	19(1)

In Figure 2 a typical TEM micrograph of the CaF_2 NPs is shown, together with the particle size distribution obtained from a statistical analysis over ca. 800 NPs. The NPs have a quite regular spherical shape, with an average particle size of 15.6 ± 3.7 nm. The size distribution can be nicely fitted to a log-normal function, as commonly observed for NPs prepared with wet-chemical techniques. The best-fit parameters give a mean diameter of 14.6 nm ($\sigma = 0.21$), in agreement with the value obtained from direct statistics (see Figure 2, inset).

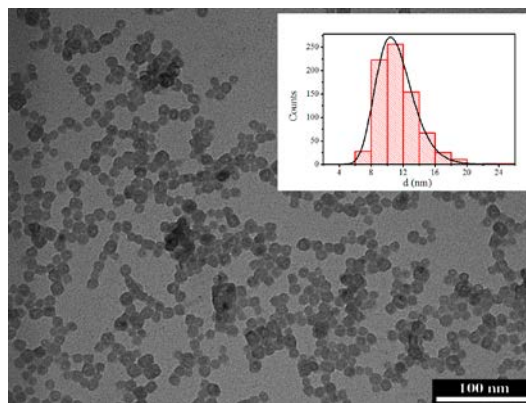


Figure 2. TEM image of the CaF_2 :Gd,Yb,Er NPs. Inset: particle size distribution histogram obtained by statistical analysis over ca. 800 NPs. Solid line: best fit curve using a log-normal distribution.

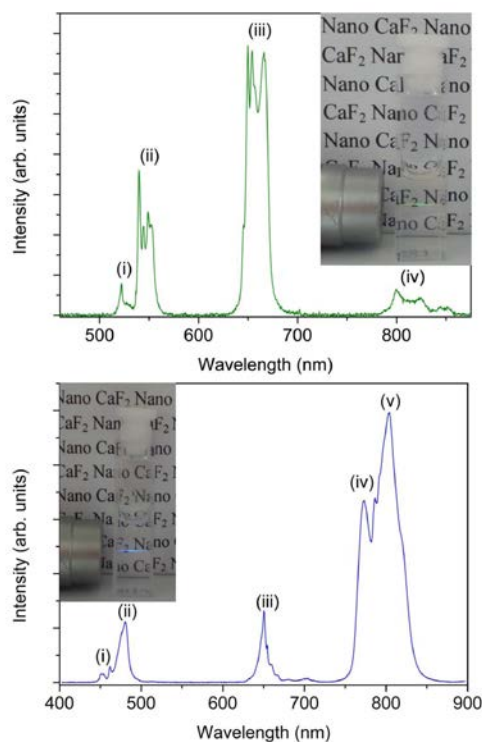


Figure 3. UC emission spectra ($\lambda_{\text{exc}}=980$ nm, laser intensity of 330 W/cm^2) for water colloidal dispersions ($\sim 1\%$ wt) of (a) CaF_2 :Gd,Yb,Er NPs (transition assignments: (i) ${}^2\text{H}_{11/2} \rightarrow {}^4\text{I}_{15/2}$; (ii) ${}^4\text{S}_{3/2} \rightarrow {}^4\text{I}_{15/2}$; (iii) ${}^4\text{F}_{9/2} \rightarrow {}^4\text{I}_{15/2}$; (iv) $({}^2\text{H}_{11/2}, {}^4\text{S}_{3/2}) \rightarrow {}^4\text{I}_{13/2}$) and (b) CaF_2 :Gd,Yb,Tm NPs (transition assignments: (i) ${}^1\text{I}_6 \rightarrow {}^3\text{H}_4$; (ii) ${}^1\text{G}_4 \rightarrow {}^3\text{H}_6$; (iii) ${}^1\text{G}_4 \rightarrow {}^3\text{F}_4$; (iv) ${}^1\text{G}_4 \rightarrow {}^3\text{H}_5$; (v) ${}^3\text{H}_4 \rightarrow {}^3\text{H}_6$).

The hydrodynamic sizes of the citrate capped NPs have been measured by the DLS technique (see Figure S1, Supporting Information) and they are 18 ± 3 nm for the CaF_2 :Gd,Yb,Er NPs and 19 ± 3 nm for the CaF_2 :Gd,Yb,Tm NPs, in perfect agreement with the average particle size and dispersion obtained by TEM images. The DLS measurements confirm that the citrate capped NPs have a very narrow size dispersion, as observed for similar NPs⁷⁹. The Zeta-potential is -19 ± 1 mV for both the NPs.

A water colloidal dispersion of the $\text{CaF}_2:\text{Gd,Er,Yb}$ NPs shows UC emission bands due to the Er^{3+} ion in the green (520-560 nm), red (640-680 nm) and infrared (790-860 nm) regions of the spectrum (Figure 3a). The red emission is much stronger than the green UC emission (the red to green intensity ratio is about 2.5). The UC spectrum of a water colloidal dispersion of the $\text{CaF}_2:\text{Gd,Yb,Tm}$ NPs (Figure 3b) shows three groups of bands in the blue (450-500 nm), red (630-670 nm) and in the NIR region around 800 nm. The infrared emission band is much stronger than the other emissions (the integrated intensity ratio is about blue:red:NIR = 1:1:4). Power studies are similar to those found in previous investigations on $\text{Er}^{3+},\text{Yb}^{3+}$ and $\text{Tm}^{3+},\text{Yb}^{3+}$ doped calcium fluoride NPs^{27,76}. In particular the UC intensity as a function of the laser intensity increases with a power higher than one, depending on the number of photons partaking the UC process. We found that the UC emissions for the water colloidal dispersions (NPs concentration of 1% wt) are easily detectable with our spectroscopic setup for excitation intensities as low as 20 and 10 W/cm^2 for the Gd,Yb,Er and Gd,Yb,Tm doped CaF_2 NPs, respectively.

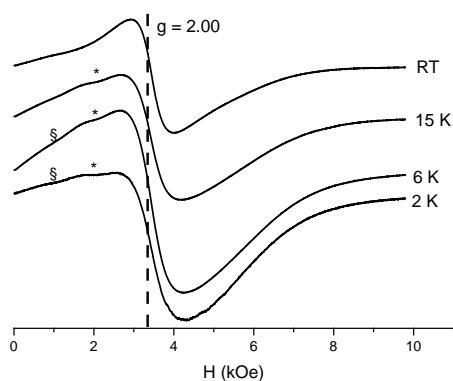


Figure 4. Temperature dependence of X-band (9.40 GHz) EPR spectrum for the $\text{CaF}_2:\text{Gd,Yb,Er}$ NPs. The dotted line corresponds to $g=2.00$ resonance field (the symbols § and * denote the resonances assigned to Er^{3+} and Yb^{3+} , respectively).

In order to get information on the magnetic properties of the NPs under investigation, EPR spectra and magnetic susceptibilities were measured. EPR spectra for $\text{CaF}_2:\text{Gd,Yb,Er}$ NPs at different temperatures are dominated by a signal centered at $g=2.00$ which behaves as a superparamagnetic one (Figure 4). Indeed, on decreasing temperatures the peak shifts

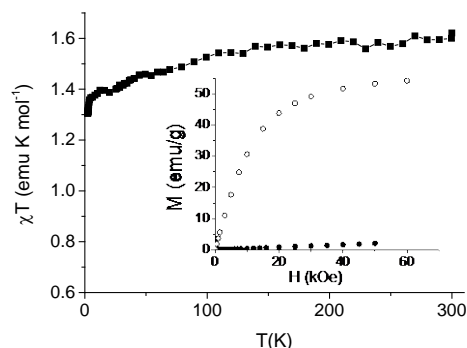


Figure 5. Temperature dependence of the χT product of $\text{CaF}_2:\text{Gd,Yb,Er}$ NPs, measured with an applied field of 1 kOe. Inset: isothermal magnetization curves measured at 2.5 K (open symbols) and 300 K (full symbols) for $\text{CaF}_2:\text{Gd,Yb,Er}$ NPs.

to low field and becomes progressively broader^{80,81}, suggesting clustering of Gd^{3+} ions in the NPs, in agreement with the X-ray analysis. At low temperature, low field shoulders can be attributed to signals of Er^{3+} and Yb^{3+} ions in cubic symmetry occurring at about $g=6.7$ and 3.4 , respectively. These signals are more evident in samples containing lower amounts of Gd^{3+} ions (see Figure S2, Supporting Information) and confirm that these ions are in substitutional position in the CaF_2 lattice⁸²⁻⁸⁴.

The temperature dependence of the χT product (shown in Figure 5) follows the expected behavior for a system containing orbitally degenerate lanthanide ions, slowly decreasing with decreasing temperature due to crystal field effect. The room temperature value, $1.60 \text{ emu K mol}^{-1}$ is close to that expected on the basis of the Curie constant of the rare earth ions weighted for their molar ratios ($1.8 \text{ emu K mol}^{-1}$). Accordingly, the field dependent magnetization measured at 2.5 K, at 6 Tesla reaches 54.2 emu/g (Figure 5) which is only slightly lower than the value calculated assuming an isotropic $g=2.00$ with $S=7/2$ for Gd^{3+} and an effective spin $S=1/2$ with $g=3.43$ and 6.7 for Yb^{3+} and Er^{3+} , respectively, as obtained by EPR spectroscopy.

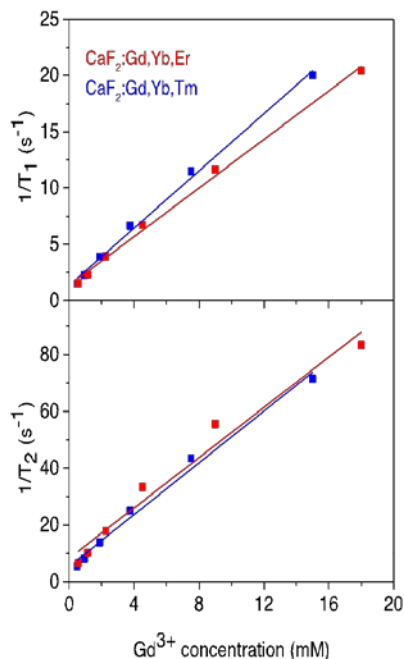
At room temperature the magnetization increases linearly with the magnetic field, as indeed expected for an assembly of paramagnetic ions, reaching 2.1 emu/g at 50 kOe. The $\text{CaF}_2:\text{Gd,Yb,Tm}$ NPs display a similar field dependent magnetization, (at 50 kOe it reaches 45.1 and 1.7 emu/g at 2.5 and 300 K, respectively, Figure S3, Supporting Information). All these data confirm the incorporation of the lanthanide ion in the fluoride lattice, producing a magnetization that makes the NPs suitable for being used as contrast agent for MRI.

Table 2. Relaxivity values for the doped CaF₂ NPs.

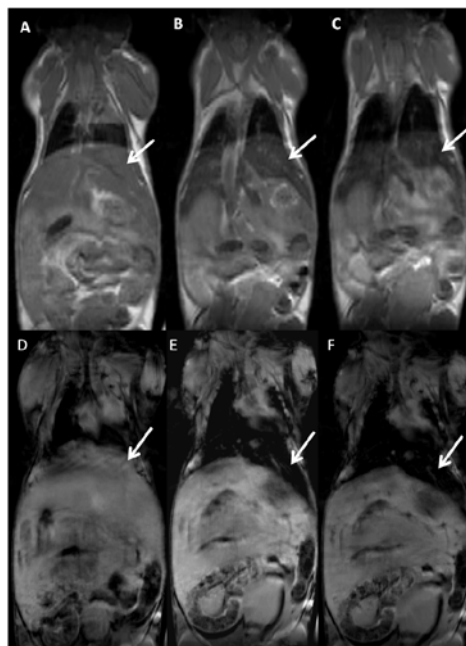
Sample	r_1 (mM ⁻¹ s ⁻¹)	r_2 (mM ⁻¹ s ⁻¹)
CaF ₂ :Gd,Er,Yb	1.1±0.2	4.4±0.2
CaF ₂ :Gd,Er,Tm	1.3±0.2	4.6±0.2

In-vitro MRI experiments were performed to measure T₁ and T₂ relaxation times of colloidal dispersions of the CaF₂:Gd,Yb,Er and CaF₂:Gd,Yb,Tm NPs vs the Gd³⁺ concentration. Figure 6 shows the 1/T₁ and 1/T₂ relaxation rates as a function of molar concentration of Gd³⁺ in the prepared dispersions. The slopes of the best fitting straight lines represent the longitudinal (r_1) and transversal (r_2) relaxivities of the NPs and the results are reported in Table 2. The obtained values of r_2 are similar to those found for Gd-DTPA and for other Gd-containing NPs⁸⁵. The r_2/r_1 ratio is about 4, conferring to these substances the property of T₂-relaxing contrast agents.

For *in-vivo* experiments, MRI images of mice before and at different time after NPs intravenous administration were acquired. For this experiment, we used the CaF₂:Gd,Yb,Tm NPs which shows a slightly higher r_2 relaxivity (see Table 2). Representative T₂ and T₂* weighted images in the coronal

**Figure 6.** Longitudinal and transverse relaxation times as a function of the Gd³⁺ concentration for the CaF₂:Gd, Yb, Er and CaF₂:Gd, Yb, Tm NPs.

plane are shown in Figure 7. It is clearly apparent that the signal intensity of the liver strongly decreases after the NPs injection indicating that the NPs are accumulating in this organ and therefore indicating that the present NPs could be used as T₂-relaxing MRI contrast agent. Moreover significant amount of NPs are also found in spleen (see Figure 8), as also reported in literature for different NPs^{9,19,20,86-88}.

**Figure 7.** MRI mouse images before (A and D) and 20 min (B and E) and 40 min (C and F) after intravenous injection of CaF₂:Gd,Yb,Tm NPs using T₂-weighted (upper panel) and T₂*-weighted sequences (lower Panel). The loss of signal intensity in the liver 40 min after NPs injection is well visible and is indicated by white arrows. The loss of signal is appreciable in particular using T₂* sequences

It is worth to remark that the group of five animals housed in controlled environment does not show any sign of mortality or modification of the daily life behavior for at least one month after the intravenous injection of the present NPs.

**Figure 8.** MRI mouse images before and after the injection of CaF₂:Gd,Yb,Tm NPs using T₂-weighted sequences. The loss of signal intensity of spleen after NPs injection is well visible and is indicated by white arrows.

In order to demonstrate the suitability of these materials for optical imaging at high spatial resolution, experiments were carried out using the liver and a piece of epithelial tissue of the mouse previously investigated by MRI. Figures 9(a) and 9(b) show images of excised mouse liver tissue upon illumination with a 980 nm diode laser beam. As revealed by this images, a green-yellow spot is clearly visible in the dark, due to the UC

emission of the $\text{CaF}_2\text{:Gd,Yb,Er}$ NPs which have been accumulated in the liver after the intravenous injection.

In order to maximize the UC signal while maintaining a sufficiently low laser power to avoid the damage of the tissue, we used a laser beam modulated by a chopper. In fact, Zhna et al.⁸⁹ demonstrated that with a modulated laser beam in the microsecond or millisecond time region it is possible to drastically reduce the average laser intensity on the sample, while maintaining the same UC detectability.

In the present setup, we used a chopper modulated at 100 Hz.

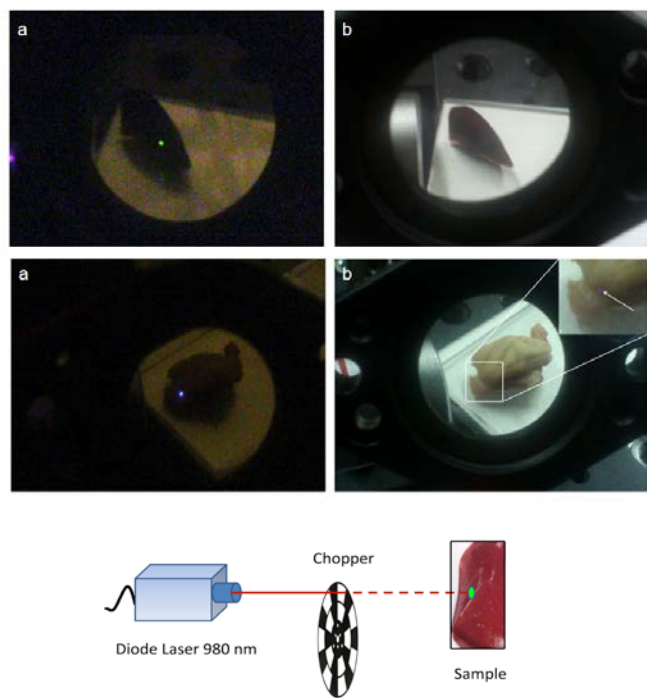


Figure 9. Upper figures: images of mouse excised liver (size of about 2 cm) in dark (a) and in ambient light (b) (excited with a 980 nm laser). Lower figures: images of an excised epithelial tissue (size of about 3 cm) in dark conditions (a) and in ambient light (b) (excited with a 980 nm laser). A 900 nm short-pass filter was used to cut the laser scattered light. A chopper modulated at 100 Hz was used.

Although in ambient light illumination the UC green spot appears not very bright (see Figure 9b), under dark conditions we were able to clearly observe the spot with the naked eye for quite low laser intensities around 46 W/cm^2 (with chopped laser exciting radiation, see Figure 9a, upper figure). Therefore, this behavior suggests the use of the present calcium fluoride NPs in clinical surgery, with the aid of a cheap 980 nm laser pointer. Moreover, the $\text{CaF}_2\text{:Gd,Yb,Tm}$ NPs were subcutaneously injected (about 3 mm in depth) in mice and the excised epithelial tissue was illuminated by a 980 nm diode laser. Pictures in the dark and in ambient light illumination for the epithelial tissue are shown in Figure 9(c) and 9(d), respectively. A bluish spot is clearly visible in both cases with the naked eye for laser intensity as low as 16 W/cm^2 (with chopped laser exciting radiation, see Figure 9a, lower figure). Even if the NIR

emission at 800 nm is not visible with the digital camera, this behavior demonstrates the practical possibility of real time optical imaging of the Tm^{3+} doped NPs with a low-power NIR laser for the clinical treatment of sub-tissue local lesions and tumors. A brighter spot, due to the 800 nm emission of Tm^{3+} ions in the NPs, would be much more visible using an infrared

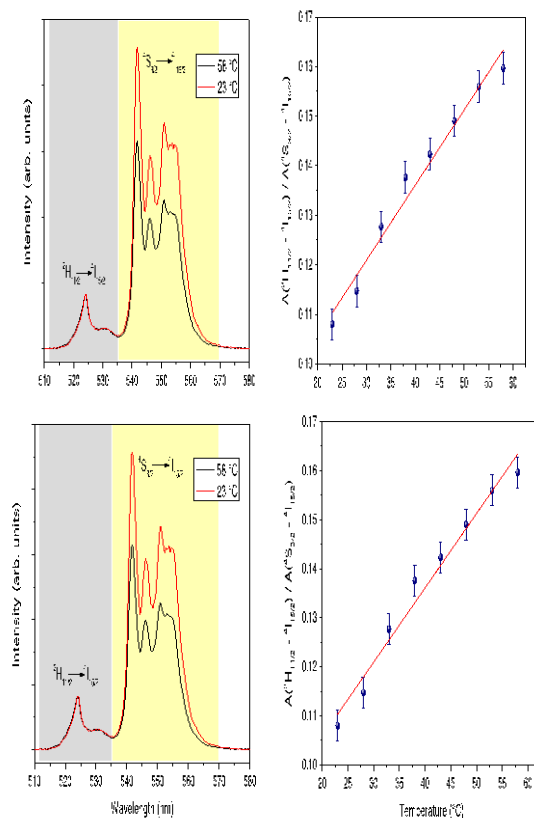


Figure 10. Upper: UC emission spectra at two different temperatures for the $\text{CaF}_2\text{:Gd,Yb,Er}$ NPs accumulated in the excised liver (excitation with a 980 nm laser). Lower: temperature dependence of the ratio of the integrated ${}^2\text{H}_{11/2} \rightarrow {}^4\text{I}_{15/2}$ (grey region) and ${}^4\text{S}_{3/2} \rightarrow {}^4\text{I}_{15/2}$ (yellow region) UC emissions.

camera.

Recent investigations have demonstrated that the monitoring of the temperature is an important issue in the use of therapeutic materials, also in nanometer size, which base their effect on hyperthermia^{90,91}. For this reason, investigation in nanothermometry has been rapidly increased in the last few years for its importance in biomedicine⁹²⁻⁹⁴. In this respect, lanthanide doped (for instance with Er^{3+} , Tm^{3+} , Nd^{3+} , Gd^{3+}) NPs have been demonstrated to be in principle very useful to monitor the local temperature both *in-vitro* and *in-vivo*^{27,95,96}. In particular, $\text{Er}^{3+}/\text{Yb}^{3+}$ doped UCNPs have been demonstrated to be particularly useful for nanothermometry⁹⁷. For the Er^{3+} lanthanide ion, the mechanism for thermometry is based on the thermalization of the two closely spaced ${}^2\text{H}_{11/2}$ and ${}^4\text{S}_{3/2}$ energy

levels of the Er^{3+} ion, and emissions from these two levels can be used for measuring the local temperature. The thermal sensitivity S for the optical temperature sensor is calculated as the rate at which the experimental variable R changes with the temperature of the host matrix, as indicated by the equation^{94,98,99}:

$$S = \frac{dR}{dT} \quad (1)$$

The possible use of near infrared radiation at 980 nm as exciting source to generate UC emission for in-vivo optical bioimaging is still under discussion. In fact, water exhibits an optical absorption band at a wavelength around 1000 nm. The absorbed light energy would induce local heating and eventually cell and tissue damage under continuous irradiation¹⁰⁰. In order to shed light into this issue, we carried out an analysis of the temperature changes induced by the 980 nm diode laser radiation directly to the liver tissue. First, we measured the temperature calibration curve for our present $\text{CaF}_2:\text{Gd,Er,Yb}$ NPs by monitoring the UC integrated

intensities of the ${}^2\text{H}_{11/2} \rightarrow {}^4\text{I}_{15/2}$ and ${}^4\text{S}_{3/2} \rightarrow {}^4\text{I}_{15/2}$ transitions of the Er^{3+} ions, as shown in Figure 10. The relative changes of the UC intensity as a function of the temperature for the two groups of bands located around 550 nm and 525 nm are clearly observable, and from a linear fit of the integrated UC intensities vs temperature (in the 25-60 °C range), we obtain a thermal sensitivity (as defined in eq. 1) of $(15.2 \pm 1.0) \cdot 10^{-4} \text{ K}^{-1}$. This value is in general similar to those observed for several Er^{3+} doped glass and glass-ceramics and it is even better than the RT value found for a fluorozirconate glass host, as reported recently by Lavin et al.¹⁰¹.

The UC spectra for the $\text{CaF}_2:\text{Gd,Er,Yb}$ NPs accumulated in the mouse excised liver are clearly visible upon excitation with a 100 Hz modulated diode laser 980 nm radiation beam, with an average power of 46 W/cm^2 (see Figure 11). A slight but significant change of the relative intensities of the UC bands is observed as a function of the irradiation time, as shown in Figure 11. Using the temperature calibration curve, a local heating is observed. Nonetheless, the variation of the local temperature is around 2-3 °C after 1 minute and around 10-12 °C after 4 minutes of continuous laser irradiation, shown in Figure 11, starting from a room temperature value of 22 °C. This temperature behavior is also confirmed by temperature measurements of the same biological tissue with comparable experimental conditions using an infrared camera (see Figure 12 as an example). All images are shown in Figure S4, (Supporting Information). Using the infrared camera, it was observed that the temperature on the surface of the biological tissue is similar to that induced by the 980 nm radiation, monitored by the UC emission, therefore corroborating the spectroscopic results. It was observed that the temperature does not increase linearly with the irradiation time but rather tends to a limiting value (see Figure 11).

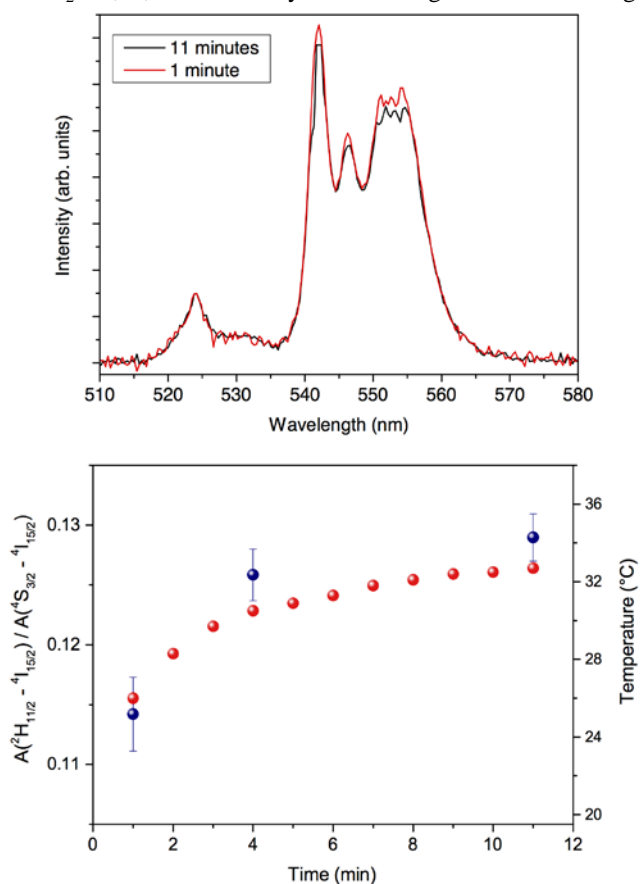


Figure 11. Upper: UC spectra for the $\text{CaF}_2:\text{Gd,Yb,Er}$ NPs in the excised liver (excitation with a 980 nm laser) for two different irradiation times. Lower: blue solid dots: time dependence of the ratio of the integrated ${}^2\text{H}_{11/2} \rightarrow {}^4\text{I}_{15/2}$ and ${}^4\text{S}_{3/2} \rightarrow {}^4\text{I}_{15/2}$ UC and the temperature calculated by the calibration curve shown in Figure 10; red solid dots: time dependence of the temperature as measured by the IR camera on the same sample under the same excitation conditions.

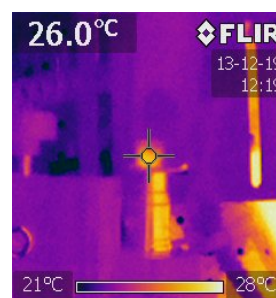


Figure 12. Infrared camera picture for the $\text{CaF}_2:\text{Gd,Yb,Er}$ NPs in a cuvette (seen from above)

After 11 minutes of continuous irradiation, the temperature has raised to 32-33 °C, around 12 °C higher than the starting temperature before the irradiation (room temperature of 22 °C). These results highlighted that although a local heating is observed, it can be limited to a raise of 1-2 °C in few seconds of laser irradiation at relatively low power, a time which is surely enough to monitor the presence of the NPs during a clinical surgery, for instance with the aid of a cheap 980 nm laser pointer.

Moreover, through careful working conditions, it would be possible to induce (and possibly monitor) a local heating by controlling the time of direct exposure of a focused laser radiation at 980 nm on the biological tissue, with a very high spatial resolution (around $500 \mu\text{m}^2$), for instance to induce cancer cell death or cauterizing the tissue during a clinical surgery.

Two-photon images of surgical samples of the mouse liver upon excitation at 975 nm are shown in Figure 13 (first channel: Figure 13(a); second channel: Figure 13(b)). The merge of the two channels highlights the co-localization of the two signals revealing the presence of the NPs in the liver (Figure 13(c)).

From the pictures it is possible to observe the localization of the NPs mainly in the blood vessels, although a small amount of NPs is also visible in the interstitial spaces suggesting the initial process of extravasation.

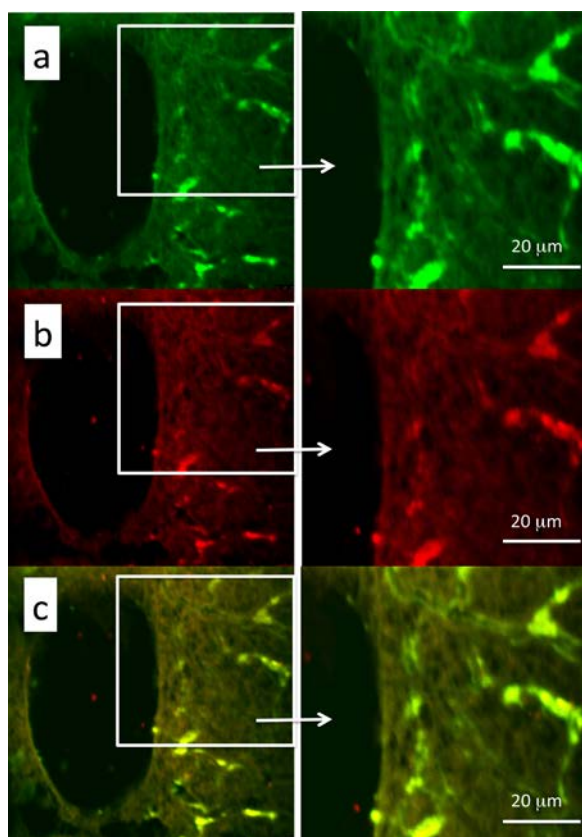


Figure 13. Two-photon images of mouse liver after 40 min from intravenous injection of $\text{CaF}_2\text{:Gd,Er,Yb}$ NPs ($\lambda_{\text{exc}} = 975$ nm). The emission radiation was collected in two channels, in 500-600 nm (a) and 600-700 nm (b) ranges. (c): merge of the two channels.

TEM images of the mouse liver tissue are shown in Figure 14 and Figure 15. Figure 14 (panel C), shows preferential localization of NPs at the level of the sinusoids within the Kupffer cells. Figure 14 (panel A) shows scarce uptake of NPs to hepatocytes probably due to a relatively short time interval elapsed after the intravenous injection. These findings suggest

that a time interval of 40 min is enough for the NPs to reach the liver but not for appreciable internalization in the hepatocytes. Ultrastructural data shown in Figure 14 a) suggest that NPs are internalized in the Kupffer cells after their adhesion to the membrane and subsequent transport into the cytoplasm where they are enveloped by membranes. Within the Kupffer cells, NPs are preferentially organized in clusters having sizes of the order of few microns. Within these clusters, it is possible to detect materials with an intermediate-electron density, which could correspond to polysaccharides. It is important to underline that hepatocytes did not show degenerative aspects nor atypical phenotype.

Careful examination of TEM images indicated that, within the present experimental conditions, the NPs are characterized by low hepatotoxicity since they do not cause cellular suffering with the exception of a modest appearance of swelling in the mitochondria when NPs clusters are considerably large (see Figure 15, panel C). Toxicity tests using the $\text{CaF}_2\text{:Gd,Yb,Tm}$ NPs on He-La cells are shown in Figure S5 for different

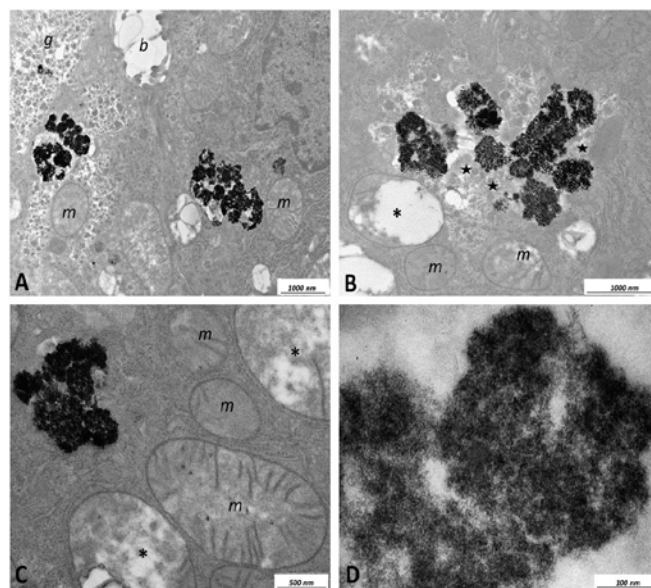


Figure 14. TEM images of ultrathin unstained sections of excised liver. A) Hepatocytes with cytoplasmic inclusions containing NPs. B-D) High magnifications of the inclusions. Legend: b: bile canaliculus; g: glycogen; m: mitochondrion; *: mitochondrion showing alteration; stars: material with moderate electron density associated to NPs.

dilutions of the NPs. The obtained results indicate that the NPs are characterized by low toxicity on the He-La cultured cells. In fact, for a 1:20 diluted dispersion, the percentage of living cells is of 77%, while for a 1:50 diluted dispersion the percentage increased reaching 85% of living cells after 6 hours of incubation.

To investigate whether NPs induce the activation of immune system, we analyzed their effects on human dendritic cells, which play an essential role in regulation of immunity⁶⁸. First of all we determined whether NPs exert toxic effects on these cells. For this purpose, human blood monocytes were cultured

for 5 days with GM-CSF and IL-4 to obtain DCs that were then challenged with NPs or with 100 ng/ml *lipopolysaccharide* (LPS), a well-known bacterial immune cells activator, as a control. The results, shown in Figure 16, clearly indicate that only extremely high doses of NPs affected DCs viability, as assessed by Annexin V staining. Similar results have been obtained upon human monocytes challenge with NPs (results not shown). It is worth to note that NP doses higher than 200 $\mu\text{g/ml}$ greatly exceed the ones commonly used for *in vitro* studies. Moreover, it is very unlikely that such high doses of NPs could reach the cells upon *in vivo* administration and have a chance to induce toxic effects. However it is possible that several injections in the patients could lead to NP accumulation in tissues, causing unwanted effects. This possibility remains to be investigated, but in this case our NPs should be preferentially used for diagnostic purposes requiring the

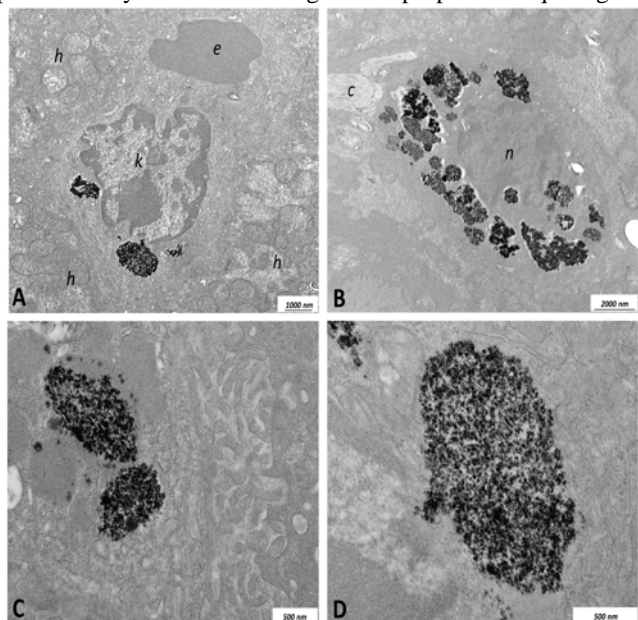


Figure 15. TEM images of ultrathin unstained sections of excised liver. A) Kupffer cell showing large cytoplasmic inclusions containing NPs. B) Macrophagic element showing large cytoplasmic inclusions containing NPs. C) and D) High magnifications of the inclusions containing NPs. C) and D) High magnifications of the inclusions. Legend: c: collagen; e: erythrocyte; k: Kupffer cell; h: hepatocyte; n: nucleus.

administration of limited amounts of NPs rather than for other medical treatments requiring the injection of several NP doses. Future studies would also be undertaken to modify NP surface (for instance by means of a different surface coating) in order to reduce their cytotoxicity {Nam2103:hw}.

The activation of DCs results in the production of various cytokines that stimulate the inflammatory process and the immune response⁷⁵. Therefore it is important to assess whether nanostructures that have to be used for medical applications stimulate these cells causing inflammation and/or adverse immune reactions once injected in patients⁶⁴. We then examined whether our NPs induce pro-inflammatory cytokine secretion by cultured human DCs by ELISA assay. We found

that NPs did not elicit the release of IL-12, IL-23, IL-1 β , IL-6 or TNF- α by DCs, as shown in Figure 17. Similar results have been obtained by treating human monocytes with NPs (results not shown). It has been reported that the blockade of the above mentioned cytokine signaling is effective in treating experimental models of autoimmune and chronic inflammatory diseases such as inflammatory bowel diseases, diabetes, multiple sclerosis, asthma and rheumatoid arthritis¹⁰²⁻¹⁰⁶. Therefore, the result that NPs do not induce the secretion of these cytokines is relevant because it indicates that the NPs are most probably immunologically inert and unable to cause harmful inflammatory responses. Moreover, this finding demonstrates that NPs are not contaminated by microorganisms or their derivatives able to induce unwanted immune reactions¹⁰⁷.

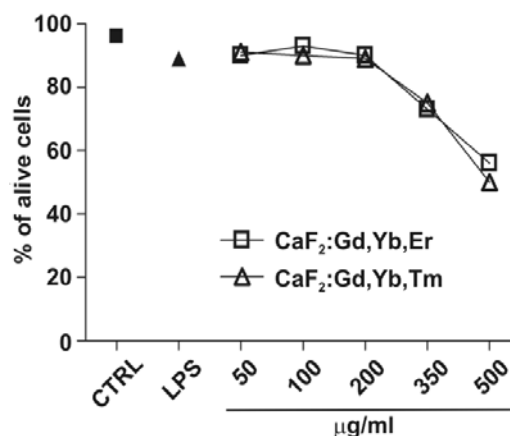


Figure 16. Effect of the CaF₂ NPs on DC viability. Monocytes were treated for 5 days with 50 ng/ml GM-CSF and 20 ng/ml IL-4 to obtain immature DCs, that were subsequently cultured in the absence (CTRL) or presence of the indicated doses of NPs. DCs were also cultured with 100 ng/ml LPS as positive control. After 24 hours cells were harvested and analyzed for their viability by Annexin V staining and subsequently by flow cytometric analysis. The graph shows the percentage of Annexin V-negative cells (alive cells) of one experiment representative of three.

4. Conclusions

Calcium fluoride NPs doped with Gd³⁺, Er³⁺, Yb³⁺ or Gd³⁺, Tm³⁺, Yb³⁺ have been prepared for the first time in colloidal form in water solutions. The hydrophilic citrate moiety bound on the particle surface guarantees the easy dispersibility in water. UC emission in the visible and infrared regions is clearly visible to the naked eye for excitation intensities as low as 10 W/cm². Magnetic measurements suggest clustering of the Gd³⁺ ions in the crystal structure. *In-vivo* MRI experiments with mice

show that after 40 minutes from the intravenous injection, the CaF₂ NPs are localized in the liver and in the spleen as

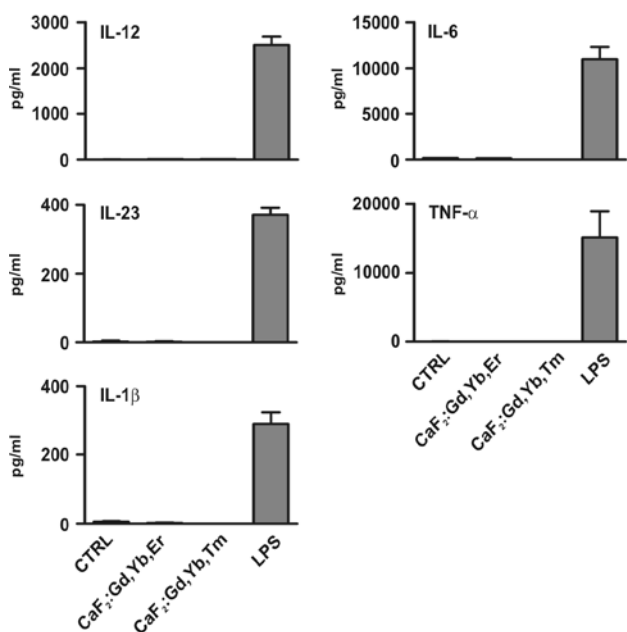


Figure 17. Effect of CaF₂ NPs on dendritic cells (DC) cytokine secretion. DCs obtained as described in Figure 11 were cultured for 24 hours in the absence (CTRL) or presence of 50 µg/ml of the NPs. DCs were also cultured with 100 ng/ml LPS as positive control. The release of the indicated cytokines in culture supernatants was evaluated by ELISA assay. Results are expressed as the mean value + SD of three independent experiments.

demonstrated by the observed substantial decrease of the MRI signal in these organs. Two-photon microscopy images of surgical samples of mouse liver confirm the presence of the NPs mainly in the blood vessels. Transmission electron microscopy images of the liver tissue confirm that the NPs have preferential localization at the level of sinusoids within the Kupffer cells. Within the Kupffer cells, the NPs are organized in clusters with sizes of few microns. The NPs are clearly observable with the naked eye in the excised liver of the mouse using with a low power diode laser at 980 nm, suggesting that the present NPs can be used in clinical surgery.

It has been demonstrated that the local heating induced by a diode laser at 980 nm at 46 W/cm² increases the local temperature of the biological tissue of around 1-2 °C if the radiation exposure time is limited up one minute, a time that could be enough to guide the surgery. These results clearly indicate that the NPs under investigation are suitable candidates to be efficiently used as bimodal probes for *in-vivo* optical and magnetic resonance imaging and medical surgery. Moreover, it is worth to remark that biocompatibility is a very important feature that needs to be fulfilled for possible *in-vitro* and *in-vivo* biomedical applications, such as multimodal imaging. To this respect, the present NPs are not toxic on both He-La cells and immune cells. In particular, the NPs did not activate human dendritic cell and monocyte response indicating that these

nanostructures do not elicit unwanted immune and inflammatory reactions. It is worth to remark that no sign of mortality or modification of the daily life status (body temperature, weight, nutritional state) for at least one month after an intravenous injection of the present NPs in a group of five mice has been observed. We are therefore confident that the investigated NPs could be considered as biocompatible multimodal imaging contrast agents.

ACKNOWLEDGEMENTS

Marzia Cerpelloni (Università di Verona, Verona, Italy) is acknowledged for expert technical support. Stefano Tambalo (Università di Verona, Verona, Italy) is gratefully acknowledged for help with measurements with the infrared camera. This work was supported by Fondazione Cariverona (Verona, Italy), project “Verona Nanomedicine Initiative” and by MIUR through FIRB project RBAP114AMK - R.I.N.A.M.E. “Rete Integrata per la Nanomedicina”. C. S., C. I. and E. F. thank the INSTM-Regione Lombardia (Italy) MAG-NANO project for partly supporting the research.

Notes and references

^a Dipartimento di Biotecnologie, Università di Verona and INSTM, Udr Verona, Strada le Grazie 15, 37134, Verona, Italy

^b Dipartimento di Informatica, Università di Verona and INSTM, Udr Verona, Strada le Grazie 15, 37134, Verona, Italy

^c Dipartimento di Scienze Neurologiche e del Movimento, Università di Verona, Piazzale L.A. Scuro 10, 37134, Verona, Italy

^d Dipartimento di Sanità Pubblica e Medicina di Comunità, Università di Verona, Piazzale L.A. Scuro 10, 37134, Verona, Italy

^e Dipartimento di Patologia e Diagnostica, Sezione di Patologia Generale, Università di Verona, Strada Le Grazie, 8, 37134, Verona, Italy

^f INSTM and Dipartimento di Chimica “U. Schiff”, Università degli Studi di Firenze, via della Lastruccia 3-13, Sesto Fiorentino, 50019, Firenze, Italy

^g ICCOM-CNR & INSTM via Madonna del Piano 10, 50019 Sesto Fiorentino (Italy)

Electronic Supplementary Information (ESI) available: DLS measurements, EPR spectrum, magnetization curves, infrared camera pictures, toxicity tests on He-La cells. See DOI: 10.1039/b000000x/

References

1. A. Louie, *Chem. Rev.*, 2010, **110**, 3146–3195.
2. W. Wu, J. Shen, P. Banerjee, and S. Zhou, *Adv. Funct. Mater.*, 2011, **21**, 2830–2839.
3. L. Cheng, K. Yang, Y. Li, J. Chen, C. Wang, M. Shao, S.-T. Lee, and Z. Liu, *Angew. Chem.*, 2011, **123**, 7523–7528.
4. M. Perfézou, A. Turner, and A. Merkoçi, *Chem. Soc. Rev.*, 2012, **41**, 2606–2622.
5. H. Kumagai, W. Pham, M. Kataoka, K.-I. Hiwatari, J. McBride, K. J. Wilson, H. Tachikawa, R. Kimura, K. Nakamura, E. H. Liu, J. C. Gore, and S. Sakuma, *Int. J. Cancer*, 2013, **132**, 2107–2117.

6. M. Asadian-Birjand, A. Sousa-Herves, D. Steinhilber, J. C. Cuggino, and M. Calderon, *Curr. Med. Chem.*, 2012, **19**, 5029–5043.
7. L. Wang, H. Xing, S. Zhang, Q. Ren, L. Pan, K. Zhang, W. Bu, X. Zheng, L. Zhou, W. Peng, Y. Hua, and J. Shi, *Biomaterials*, 2013, **34**, 3390–3401.
8. Y. Li, G. H. Gao, and D. S. Lee, *Adv. Healthc. Mater.*, 2012, **2**, 388–417.
9. C. Liu, Z. Gao, J. Zeng, Y. Hou, F. Fang, Y. Li, R. Qiao, L. Shen, H. Lei, W. Yang, and M. Gao, *ACS Nano*, 2013, 130726154521000.
10. L. M. Maestro, E. M. Rodríguez, F. Vetrone, R. Naccache, H. L. Ramirez, D. Jaque, J. A. Capobianco, and J. G. Solé, *Opt. Express*, 2010, **18**, 23544–23553.
11. H. B. Na, I. C. Song, and T. Hyeon, *Adv. Mater.*, 2009, **21**, 2133–2148.
12. F. Evanics, P. R. Diamente, F. C. J. M. van Veggel, G. J. Stanisz, and R. S. Prosser, *Chem. Mater.*, 2006, **18**, 2499–2505.
13. T. Passuello, M. Pedroni, F. Piccinelli, S. Polizzi, P. Marzola, S. Tambalo, G. Conti, D. Benati, F. Vetrone, M. Bettinelli, and A. Speghini, *Nanoscale*, 2012, **4**, 7682–7689.
14. P. Marzola, F. Osculati, and A. Sbarbati, *Eur. J. Radiol.*, 2003, **48**, 165–170.
15. S. V. Eliseeva and J.-C. G. Bünzli, *Chem. Soc. Rev.*, 2009, **39**, 189–227.
16. M. D'Onofrio, E. Gianolio, A. Ceccon, F. Arena, S. Zanzoni, D. Fushman, S. Aime, H. Molinari, and M. Assfalg, *Chem.-Eur. J.*, 2012, **18**, 9919–9928.
17. F. Wang and X. Liu, *Chem. Soc. Rev.*, 2009, **38**, 976–989.
18. F. Wang, Y. Han, C. S. Lim, Y. Lu, J. Wang, J. Xu, H. Chen, C. Zhang, M. Hong, and X. Liu, *Nature*, 2010, **463**, 1061–1065.
19. Q. Liu, Y. Sun, C. Li, J. Zhou, C. Li, T. Yang, X. Zhang, T. Yi, D. Wu, and F. Li, *ACS Nano*, 2011, **5**, 3146–3157.
20. Y. Sun, X. Zhu, J. Peng, and F. Li, *ACS Nano*, 2013, **7**, 11290–11300.
21. D. Ni, J. Zhang, W. Bu, H. Xing, F. Han, Q. Xiao, Z. Yao, F. Chen, Q. He, J. Liu, S. Zhang, W. Fan, L. Zhou, W. Peng, and J. Shi, *ACS Nano*, 2014, 140113090916002.
22. D. Tu, Y. Liu, H. Zhu, and X. Chen, *Chem.-Eur. J.*, 2013, **19**, 5516–5527.
23. F. Vetrone and J. A. Capobianco, *Int. J. Nanotechnol.*, 2008, **5**, 1306–1339.
24. F.-F. Chen, Z.-Q. Chen, Z.-Q. Bian, and C.-H. Huang, *Coord. Chem. Rev.*, 2010, **254**, 991–1010.
25. R. Kumar, M. Nyk, T. Y. Ohulchanskyy, C. A. Flask, and P. N. Prasad, *Adv. Funct. Mater.*, 2009, **19**, 853–859.
26. L. Cheng, C. Wang, and Z. Liu, *Nanoscale*, 2012.
27. N.-N. Dong, M. Pedroni, F. Piccinelli, G. Conti, A. Sbarbati, J. E. Ramírez-Hernández, L. M. Maestro, M. C. Iglesias-de la Cruz, F. Sanz-Rodríguez, A. Juarranz, F. Chen, F. Vetrone, J. A. Capobianco, J. G. Solé, M. Bettinelli, D. Jaque, and A. Speghini, *ACS Nano*, 2011, **5**, 8665–8671.
28. F. Vetrone, R. Naccache, A. Juarranz de la Fuente, F. Sanz-Rodríguez, A. Blazquez-Castro, E. Martin Rodriguez, D. Jaque, J. Garcia Sole, and J. A. Capobianco, *Nanoscale*, 2010, **2**, 495–498.
29. S. Aime, F. Fedeli, A. Sanino, and E. Terreno, *J. Am. Chem. Soc.*, 2006, **128**, 11326–11327.
30. J. L. Major and T. J. Meade, *Acc. Chem. Res.*, 2009, **42**, 893–903.
31. M. Ahren, L. Selegard, A. Klason, F. Soderlind, N. Abrikosova, C. Skoglund, T. Bengtsson, M. Engstrom, P.-O. Kall, and K. Uvdal, *Langmuir*, 2010, **26**, 5753–5762.
32. G. K. Das, B. C. Heng, S.-C. Ng, T. White, J. S. C. Loo, L. D'Silva, P. Padmanabhan, K. K. Bhakoo, S. T. Selvan, and T. T. Y. Tan, *Langmuir*, 2010, **26**, 8959–8965.
33. T. Paik, T. R. Gordon, A. M. Prantner, H. Yun, and C. B. Murray, *ACS Nano*, 2013, **7**, 2850–2859.
34. W. Ren, G. Tian, L. Zhou, W. Yin, L. Yan, S. Jin, Y. Zu, S. Li, Z. Gu, and Y. Zhao, *Nanoscale*, 2012, **4**, 3754–3760.
35. T. Grzyb, A. Gruszczka, R. J. Wiglusz, Z. Śniadecki, B. Idzikowski, and S. Lis, *J. Mater. Chem.*, 2012, **22**, 22989–22997.
36. W. Yin, L. Zhou, Z. Gu, G. Tian, S. Jin, L. Yan, X. Liu, G. Xing, W. Ren, F. Liu, Z. Pan, and Y. Zhao, *J. Mater. Chem.*, 2012, **22**, 6974–6981.
37. M. Botta, L. Tei, F. Carniato, and T. Kalavani, *J. Mater. Chem.*, 2013, **1**, 2442–2446.
38. S. Rodríguez-Liviano, N. O. Nuñez, S. Rivera-Fernández, J. M. de la Fuente, and M. Ocaña, *Langmuir*, 2013, **29**, 3411–3418.
39. Y. Tian, H.-Y. Yang, K. Li, and X. Jin, *J. Mater. Chem.*, 2012, **22**, 22510–22516.
40. N. J. J. Johnson, W. Oakden, G. J. Stanisz, R. Scott Prosser, and F. C. J. M. van Veggel, *Chem. Mater.*, 2011, **23**, 3714–3722.
41. H.-T. Wong, M.-K. Tsang, C.-F. Chan, K.-L. Wong, B. Fei, and J. Hao, *Nanoscale*, 2013, **5**, 3465–3473.
42. Q. Ju, D. Tu, Y. Liu, R. Li, H. Zhu, J. Chen, Z. Chen, M. Huang, and X. Chen, *J. Am. Chem. Soc.*, 2012, **134**, 1323–1330.
43. J. Zhou, M. Yu, Y. Sun, X. Zhang, X. Zhu, Z. Wu, D. Wu, and F. Li, *Biomaterials*, 2011, **32**, 1148–1156.
44. S. Zeng, J. Xiao, Q. Yang, and J. Hao, *J. Mater. Chem.*, 2012, **22**, 9870–9874.
45. Q. Liu, Y. Sun, T. Yang, W. Feng, C. Li, and F. Li, *J. Am. Chem. Soc.*, 2011, **133**, 17122–17125.
46. J. Zhou, X. Zhu, M. Chen, Y. Sun, and F. Li, *Biomaterials*, 2012, **33**, 6201–6210.
47. W. Yin, L. Zhao, L. Zhou, Z. Gu, X. Liu, G. Tian, S. Jin, L. Yan, W. Ren, G. Xing, and Y. Zhao, *Chem.-Eur. J.*, 2012, **18**, 9239–9245.
48. J. Zhou, Y. Sun, X. Du, L. Xiong, H. Hu, and F. Li, *Biomaterials*, 2010, **31**, 3287–3295.
49. F. Liu, X. He, L. Liu, H. You, H. Zhang, and Z. Wang, *Biomaterials*, 2013, **34**, 5218–5225.
50. N. Bogdan, F. Vetrone, R. Roy, and J. A. Capobianco, *J. Mater. Chem.*, 2010, **20**, 7543–7550.
51. H.-T. Wong, F. Vetrone, R. Naccache, H. L. W. Chan, J. Hao, and J. A. Capobianco, *J. Mater. Chem.*, 2011, **21**, 16589–16596.
52. M. He, P. Huang, C. Zhang, H. Hu, C. Bao, G. Gao, R. He, and D. Cui, *Adv. Funct. Mater.*, 2011, **21**, 4470–4477.
53. F. Chen, W. Bu, S. Zhang, J. Liu, W. Fan, L. Zhou, W. Peng, and J. Shi, *Adv. Funct. Mater.*, 2012, **23**, 298–307.
54. H.-T. Wong, H. L. W. Chan, and J. Hao, *Opt. Express*, 2010, **18**, 6123–6130.
55. K. A. Abel, J.-C. Boyer, C. M. Andrei, and F. C. J. M. van Veggel, *J. Phys. Chem. Lett.*, 2011, **2**, 185–189.
56. G. Chen, T. Y. Ohulchanskyy, W.-C. Law, H. Agren, and P. N. Prasad, *Nanoscale*, 2011, **3**, 2003–2008.
57. X.-F. Qiao, J.-C. Zhou, J.-W. Xiao, Y.-F. Wang, L.-D. Sun, and C.-H. Yan, *Nanoscale*, 2012, **4**, 4611–4623.
58. F. Li, C. Li, X. Liu, Y. Chen, T. Bai, L. Wang, Z. Shi, and S. Feng, *Chem.-Eur. J.*, 2012, **18**, 11641–11646.
59. C. Dong, A. Korinek, B. Blasiak, B. Tomanek, and F. C. J. M. van Veggel, *Chem. Mater.*, 2012, **24**, 1297–1305.
60. F. Chen, W. Bu, S. Zhang, X. Liu, J. Liu, H. Xing, Q. Xiao, L. Zhou, W. Peng, L. Wang, and J. Shi, *Adv. Funct. Mater.*, 2011, **21**, 4285–4294.
61. D. Q. Chen, Y. L. Yu, F. Huang, P. Huang, A. P. Yang, and Y. S. Wang, *J. Am. Chem. Soc.*, 2010, **132**, 9976–9978.
62. F. Wang, R. Deng, J. Wang, Q. Wang, Y. Han, H. Zhu, X. Chen, and X. Liu, *Nat. Mater.*, 2011, **10**, 968–973.
63. L. W. Yang, Y. Y. Zhang, J. J. Li, Y. Li, J. X. Zhong, and P. K. Chu, *Nanoscale*, 2010, **2**, 2805–2810.
64. C. Chang, *Journal of Autoimmunity*, 2010, **34**, J234–J246.
65. D. Yang, Y. Zhao, H. Guo, Y. Li, P. Tewary, G. Xing, W. Hou, J. J. Oppenheim, and N. Zhang, *ACS Nano*, 2010, **4**, 1178–1186.
66. M. Di Gioacchino, C. Petrarca, F. Lazzarin, L. Di Giampaolo, E. Sabbioni, P. Boscolo, R. Mariani-Costantini, and G. Bernardini, *Int. J. Immunopathol. Pharmacol.*, 2011, **24**, 65S–71S.
67. D. Segat, R. Tavano, M. Donini, F. Selvestrel, I. Rio-Echevarria, M. Rojnik, P. Kocbek, J. Kos, S. Iratni, D. Sheglmann, F. Mancin, S. Dusi, and E. Papini, *Nanomedicine*, 2011, **6**, 1027–1046.
68. F. Granucci, I. Zanoni, and P. Ricciardi-Castagnoli, *Cell. Mol. Life Sci.*, 2008, **65**, 1683–1697.
69. D. A. A. Vignali and V. K. Kuchroo, *Nat. Immunol.*, 2012, **13**, 722–728.

70. M. Xu, I. Mizoguchi, N. Morishima, Y. Chiba, J. Mizuguchi, and T. Yoshimoto, *Clin. Dev. Immunol.*, 2010, **2010**, 1–9.
71. J. K. Elmquist, T. E. Scammell, and C. B. Saper, *Trends Neurosci.*, 1997, **20**, 565–570.
72. A. F. Suffredini, G. Fantuzzi, R. Badolato, J. J. Oppenheim, and N. P. O'Grady, *J. Clin. Immunol.*, 1999, **19**, 203–214.
73. E. Gruys, M. J. M. Toussaint, T. A. Niewold, and S. J. Koopmans, *J. Zhejiang Univ. Sci.*, 2005, **6B**, 1045–1056.
74. K. Schäkel, *Experimental Dermatology*, 2009, **18**, 264–273.
75. N. Cools, A. Petrizzo, E. Smits, F. M. Buonaguro, M. L. Tornesello, Z. Berneman, and L. Buonaguro, *Immunotherapy*, 2011, **3**, 1203–1222.
76. M. Pedroni, F. Piccinelli, T. Passuello, M. Giarola, G. Mariotto, S. Polizzi, M. Bettinelli, and A. Speghini, *Nanoscale*, 2011, **3**, 1456–1460.
77. V. Petit, P. Camy, J. L. Doualan, X. Portier, and R. Moncorgé, *Phys. Rev. B*, 2008, **78**, 085131.
78. V. A. Streltsov, V. G. Tsirelson, R. P. Ozerov, and O. A. Golovanov, *Kristallografiya*, 1988, **33**, 90–97.
79. M. Pedroni, F. Piccinelli, T. Passuello, S. Polizzi, J. Ueda, P. Haro-Gonzalez, L. Martinez Maestro, D. Jaque, J. Garcia Sole, M. Bettinelli, and A. Speghini, *Cryst. Growth Des.*, 2013, **13**, 4906–4913.
80. Y. L. Raikher and V. I. Stepanov, *Sov. Phys. JETP*, 1992, **75**, 764–771.
81. M. Fittipaldi, L. Sorace, A. L. Barra, C. Sangregorio, R. Sessoli, and D. Gatteschi, *Phys. Chem. Chem. Phys.*, 2009, **11**, 6555–6568.
82. U. Ranon and W. Low, *Phys. Rev.*, 1963, **132**, 1609–1611.
83. K. I. Gerasimov and M. L. Falin, *Phys. Solid State*, 2009, **51**, 721–726.
84. I. A. Irisova, A. A. Rodionov, D. A. Tayurskii, and R. V. Yusupov, *J. Phys.: Conf. Ser.*, 2011, **324**, 012026.
85. M. Botta and L. Tei, *Eur. J. Inorg. Chem.*, 2012, **2012**, 1945–1960.
86. G. Liang, D. Ye, X. Zhang, F. Dong, H. Chen, S. Zhang, J. Li, X. Shen, and J. Kong, *J. Mater. Chem. B*, 2013, **1**, 3545–3552.
87. E. Hemmer, H. Takeshita, T. Yamano, T. Fujiki, Y. Kohl, K. Löw, N. Venkatachalam, H. Hyodo, H. Kishimoto, and K. Soga, *J Mater Sci: Mater Med*, 2012, **23**, 2399–2412.
88. C.-C. Huang, C.-Y. Tsai, H.-S. Sheu, K.-Y. Chuang, C.-H. Su, U.-S. Jeng, F.-Y. Cheng, C.-H. Su, H.-Y. Lei, and C.-S. Yeh, *ACS Nano*, 2011, **5**, 3905–3916.
89. Q. Zhan, *Theranostics*, **3**, 306–316.
90. Y. Wang, K. C. L. Black, H. Luehmann, W. Li, Y. Zhang, X. Cai, D. Wan, S.-Y. Liu, M. Li, P. Kim, Z.-Y. Li, L. V. Wang, Y. Liu, and Y. Xia, *ACS Nano*, 2013, **7**, 2068–2077.
91. Y. Jin, J. Wang, H. Ke, S. Wang, and Z. Dai, *Biomaterials*, 2013, **34**, 4794–4802.
92. C. D. S. Brites, P. P. Lima, N. J. O. Silva, A. Millán, V. S. Amaral, F. Palacio, and L. D. Carlos, *Nanoscale*, 2013, **5**, 7572–7580.
93. C. D. S. Brites, P. P. Lima, N. J. O. Silva, A. Millán, V. S. Amaral, F. Palacio, and L. D. Carlos, *New J. Chem.*, 2011, **35**, 1177–1183.
94. D. Jaque and F. Vetrone, *Nanoscale*, 2012, **4**, 4301.
95. U. Rocha, C. Jacinto da Silva, W. Ferreira Silva, I. Guedes, A. Benayas, L. Martinez Maestro, M. Acosta Elias, E. Bovero, F. C. J. M. van Veggel, J. A. García Solé, and D. Jaque, *ACS Nano*, 2013, **7**, 1188–1199.
96. K. Zheng, Z. Liu, C. Lv, and W. Qin, *J. Mater. Chem. C*, 2013, **1**, 5502–5507.
97. F. Vetrone, R. Naccache, A. Zamarron, A. Juarranz de la Fuente, F. Sanz-Rodriguez, L. Martinez Maestro, E. Martin Rodriguez, D. Jaque, J. Garcia Sole, and J. A. Capobianco, *ACS Nano*, 2010, **4**, 3254–3258.
98. X.-D. Wang, O. S. Wolfbeis, and R. J. Meier, *Chem. Soc. Rev.*, 2013, **42**, 7834–7869.
99. C. D. S. Brites, P. P. Lima, N. J. O. Silva, A. Millán, V. S. Amaral, F. Palacio, and L. D. Carlos, *Nanoscale*, 2012, **4**, 4799–4829.
100. Y. Zhong, G. Tian, Z. Gu, Y. Yang, L. Gu, Y. Zhao, Y. Ma, and J. Yao, *Adv. Mater.*, 2013.
101. S. F. León-Luis, U. R. Rodríguez-Mendoza, P. Haro-González, I. R. Martín, and V. Lavín, *Sensors and Actuators B: Chemical*, 2012, **174**, 176–186.
102. M. F. Neurath and S. Finotto, *Cytokine and Growth Factor Reviews*, 2011, **22**, 83–89.
103. M. Wong, D. Ziring, Y. Korin, S. Desai, S. Kim, J. Lin, D. Gjertson, J. Braun, E. Reed, and R. R. Singh, *Clin. Immunol.*, 2008, **126**, 121–136.
104. G. Bamias and F. Cominelli, *Curr. Opin. Pharmacol.*, 2006, **6**, 401–407.
105. A. So, A. Ives, L. A. B. Joosten, and N. Busso, *Nat. Rev. Rheumatol.*, 2013, 1–9.
106. D. De Nitto, M. Sarra, M. L. Cupi, F. Pallone, and G. Monteleone, *Curr. Pharm. Des.*, 2010, **16**, 3656–3660.
107. B. Fadeel and A. E. Garcia-Bennett, *Adv. Drug Deliv. Rev.*, 2010, **62**, 362–374.

Lanthanide doped CaF_2 nanoparticles are useful for *in-vivo* optical and MR imaging and as nanothermometer probes, which do not induce pro-inflammatory cytokine secretion by human dendritic cells.

